Geomechanics for Energy and the Environment 21 (2020) 100161

Contents lists available at ScienceDirect

Geomechanics for Energy and the Environment

journal homepage: www.elsevier.com/locate/gete

Reactive instabilities in linear acidizing on carbonates

Euripides Papamichos [a,b,*], Polyneikis Strongylis [a], Andreas Bauer [c]

[a] Department of Civil Engineering, Aristotle University of Thessaloniki, Greece
[b] SINTEF Industry, Trondheim, Norway
[c] Aker BP, Trondheim, Norway

ARTICLE INFO

Article history:
Received 18 May 2019
Received in revised form 27 November 2019
Accepted 28 November 2019
Available online 30 November 2019

Keywords:
Acidizing
Carbonates
Wormholes
Stephan problem
Linear stability analysis
Reactive instabilities

ABSTRACT

Acid injection, reactive instabilities and wormholing in carbonate reservoirs is investigated through the analysis of the linear acidizing problem theoretically and experimentally. Theoretically acidizing was analyzed by formulating the problem as a reactive moving boundary Stefan type problem. Wormholing is viewed as a reactive infiltration instability to the trivial solution of uniform dissolution. A linear stability analysis from the equilibrium state is performed and the critical wavenumber below which instabilities have a positive growth rate is identified. When applied to the scale of the experiment, an optimum injection velocity is identified for a given formation and injection concentration, for the growth for a single wormhole. This optimum injection velocity scales with the inverse of the specimen diameter. Experimentally, linear acidizing tests were performed in Mons chalk, a high porosity analogue of North Sea reservoir chalk. In the experiments the critical injection velocity for wormhole formation at minimum acid injection was obtained and the results were compared with the theoretical predictions.

1. Introduction

Matrix acidizing is a common reservoir stimulation technique in the petroleum industry aiming to recover or enhance permeability in the near wellbore region. Hydrochloric acid solutions or mixtures of hydrochloric acid with hydrofluoric acid are injected at pressures below the fracturing pressure of the formation. Acid transported by the aqueous solution reacts with the rock and dissolves it. This leads to a rock permeability increase either by removing the permeability damage caused during drilling and production or by creating new and larger pathways.[1] Acidizing is applied to both carbonate and sandstone formations; however, the process is fundamentally different in each case. Acidizing in sandstones is characterized by relatively low reaction rates leading to uniform dissolution patterns while carbonate acidizing exhibits high reaction rates leading to sharp dissolution fronts and the creation of pathways of high permeability called wormholes.[1] Fig. 1 shows a schematic of a carbonate acidizing application and the creation of wormholes.

The objective of an acidizing treatment design is to select the acid injection rate and concentration to create long and narrow wormholes thus creating pathways of increased permeability with minimum acid spent. In experiments, this translates to a quantity known as Pore Volume To Breakthrough (PVTB) meaning the number of acid solution pore volumes of the rock specimen which have to be injected before the first breakthrough from the inlet to the outlet side has been generated in a cylindrical rock specimen. The PVTB should be minimized for an optimum acidizing application. This concept has been demonstrated well by McDuff et al.[2] In the minimum PVTB value, the corresponding dissolution pattern shows a single narrow wormhole extending to the whole length of the specimen while for lower or higher values of acid injection velocity, the wormholes become either thicker or ramified, respectively.

Acidizing has received a growing interest in the last decades with researchers contributing to experimental investigations,[2–5] analytical modeling[6–8] and numerical simulations.[9–12] The experimental works generally focus on demonstrating the various dissolution patterns generated by different acid injection rates and concentrations. An important work was presented by Fredd and Fogler[3] who performed acidizing experiments with hydrochloric acid solutions injected at various values of the Damkohler number showing that for relatively low values of flow velocity, dissolution advances in a uniform manner while the increase in this parameter eventually leads to an optimum injection rate for the formation of wormholes. A further increase in flow velocity leads to ramified, dendritic structures. Experimental work revealed also a scale dependency of the optimum acid injection rate.[13] In a PVTB vs. velocity plot, the optimal velocity appears to be linearly proportional to the inverse of the sample size. An

* Correspondence to: Department of Civil Engineering, Aristotle University of Thessaloniki, GR-54124 Thessaloniki, Greece.
E-mail addresses: epapamic@civil.auth.gr (E. Papamichos), polyneik@civil.auth.gr (P. Strongylis), andreas.bauer@akerbp.com (A. Bauer).

https://doi.org/10.1016/j.gete.2019.100161

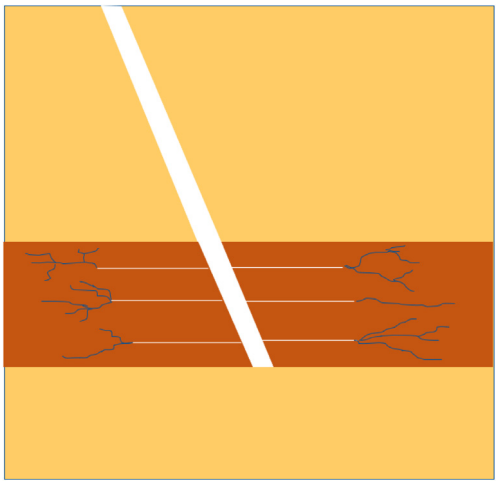

Fig. 1. Wormholes created by acid injection into a perforated completion.

analytical extraction of this scale dependency is one of the goals of the paper.

Analytical studies generally focus on the reactive infiltration instability, a phenomenon which is described in more detail in Section 2. The analysis of this instability follows the solution of a moving boundary problem and gives predictions for the critical values of the control parameters for wormhole creation and propagation.[8] The validation of the results of the linear stability analysis on experiments on carbonates can provide a method to predict the optimum injection velocity and upscale results from different specimen sizes to the field.

Numerical studies focus on the simulation of boundary value problems with fixed inlet and outlet boundaries. Some of them[12] use an averaged computational fluid mechanics approach while others[10,11] suggest a two-scale model to study the effect of medium heterogeneities to the wormhole pattern. Numerical codes can handle more complex coupled chemical reactions, and this is essential for the simulation of acidizing in sandstones.[9] All the numerical studies produce contour plots of the generated dissolution pattern and try to extract the optimum conditions to minimize the PVTB.

The theoretical work in this paper combines the results of a linear stability analysis of the acidizing process with experimental results to validate the theoretical predictions on the onset of instability and the optimum conditions for the creation of wormholes. The linear stability analysis is a useful mathematical technique that investigates the potential for onset and growth of an instability. The analysis does not attempt to model the post-bifurcation/post instability development which requires numerical methods due to the loss of uniformity. Stress, temperature or other effects are not considered in either the analysis or the experiments. The analytical approach that is presented follows concepts introduced by Ortoleva et al.[14] and later by Zhao et al.[8] and formulates the advective–dispersive–reactive transport as a moving boundary problem involving a reacted and an unreacted region. Section 2 introduces the concepts and assumptions of wormholing which is a reactive type infiltration instability encountered in carbonate acidizing and is analyzed as a perturbation to the uniform dissolution front. Section 3 describes the moving boundary problem of acid dissolution and Section 4 derives the analytical solutions for an equilibrium state corresponding to a uniform dissolution pattern. Section 5 performs a scaling process to define the internal lengths and time durations of the system and reformulates the boundary value problem to scaled, non-dimensional variables. A classical linear stability analysis is performed in Section 6. Its results are the dominant wavelengths of instability expected for various values of acid injection rates and the critical value of acid injection rate for the onset of wormhole formation for a given specimen size. These predictions are put under examination in Section 8 with the aid of experimental results from acidizing tests on Mons chalk described in Section 7 after performing the necessary scale dependent calculations. The experimental results complement the theoretical study and provide means to validate the theoretical predictions. Mons is an outcrop analogue chalk for high porosity North Sea chalk reservoirs. The experiments were performed in a Hassler cell on cylindrical specimens initially oil or brine saturated by injecting a 15% v/v HCl solution at two different injection rates. Section 9 summarizes the conclusions and discusses the predictions and the underlying assumptions of the analytical model.

2. Reactive infiltration instability

Carbonate acidizing and wormholing where an aqueous hydrochloric acid solution is injected in carbonate rocks, can be considered as a reactive infiltration instability phenomenon in the sense of the definitions set by Chadam et al.[15] Reactive infiltration instability is an example of self-organization as an autonomous passage of a system from an un-patterned state to a patterned state without externally imposing a specific template.[16] For this instability to develop and patterns to emerge, destabilizing factors, i.e. self-amplifying phenomena where forces tend to amplify a disturbance driving constantly the system out of equilibrium, dominate over the stabilizing factors, i.e. the self-equilibrating phenomena where forces tend to dampen disturbances and drive the system back to equilibrium. The interplay between these two types of phenomena under the specific initial and boundary conditions leads to a specific pattern in the domain of interest.

In reactive flow, an aqueous acid solution is injected into porous rock. The chemical species of the aqueous solution react with the rock minerals dissolving rock and thus increasing its porosity and permeability. A higher permeability causes a larger fluid flux, eventually bringing larger quantities of reactants in the aqueous solution to the areas of higher permeability. This again further increases dissolution and permeability. These are the destabilizing phenomena because an infinitesimal nonuniformity e.g. in permeability of the rock tends to be amplified by the physics of the system leading to fingering (Fig. 2a). As a result of diffusion, these fingers cannot grow indefinitely and there is a stabilizing force that limits their advancement and growth. Fig. 2b displays a higher porosity finger and shows that reactants in the aqueous solution must travel larger distances from upstream to reach the tip of the finger. During this time, they diffuse to the boundaries of the finger. The larger the finger the greater the loss of the reactant's concentration before reaching the tip. This causes the finger on one side to widen due to the reaction at the finger boundaries and on the other side to slow down the tip advancement due to poor reactant concentration at the tip. It is reasonable to expect that fingers will halt their advancement once a critical finger length has been reached where the reactant concentration at the tip vanishes. These are the stabilizing mechanisms.

Often reactive infiltration instabilities are modeled analytically as moving boundary problems where rock is separated into two distinct phases, one reacted phase which has been dissolved to its maximum porosity and one unreacted phase where rock is intact and at its initial porosity.[8,14,15] Section 3 describes the formulation of the moving boundary problem for the linear case. The important things to mention are the assumptions required to support such a formulation. First, a thin front approximation

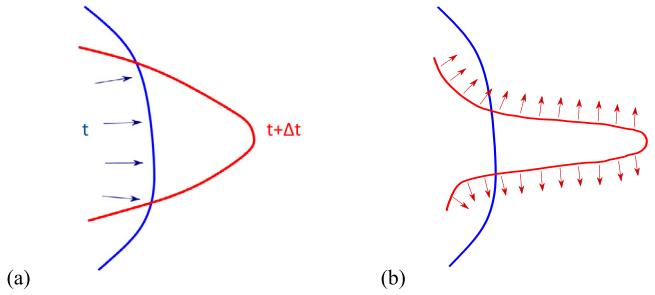

Fig. 2. (a) Destabilizing and (b) stabilizing mechanisms of reactive instability.

is made between the reacted and unreacted phases of the rock which allows a formulation like the one in the classical Stefan problem of melting of ice.[17] This assumption is based on the fact that the concentration of the reactant in the aqueous solution is several orders of magnitude smaller than the mineral density in the rock. By using a large density asymptotics assumption and several mathematical manipulations the thin reaction front postulate is inferred. However, some researchers claim that the large density asymptotics assumption is not a sufficient condition for the thin front limit and the necessary condition is the fast reaction limit.[18,19] Indeed, fast reaction rates can yield a thin front since for the movement of an infinitesimal sharp front, all the rock at the front must reach its maximum porosity and be completely dissolved during the infinitesimal time interval. Fast reaction rates, as compared to the dispersion and advection timescales, guarantee the thin reaction front. This is a different case from slow dissolution problems like weathering of calcarenites by environmental agents.[20]

As already mentioned in Section 1, carbonate acidizing exhibits high reaction rates allowing the modeling of the phenomenon as a moving boundary problem. After solving the uniform dissolution case, a confirmation of the validity of the thin front assumption is presented using calculated values of front velocity and values obtained from experiments for the acid injection rates, diffusion–dispersion coefficients and chemical reaction rates of the specific materials of this application.

3. Formulation of moving boundary problem for reactive flow

The problem is formulated for a porous rock whose representative volume V consists of solids s with volume V_s and fluid f with volume V_f. It is assumed that the fluid covers all the void space V_v, such that $V_f = V_v$. The fluid is an aqueous hydrochloric acid (HCl) solution which reacts with calcium carbonate ($CaCO_3$) according to the chemical reaction

$$CaCO_3 + 2HCl \rightarrow CaCl_2 + H_2O + CO_2 \tag{1}$$

The porous rock is a pure chalk composed of 99% calcium carbonate. It is thus considered that the only chemical reaction that takes place is the one-way reaction Eq. (1). The porosity ϕ, molar concentration c of the acid in the fluid and molar density ρ_s of the chalk are defined as

$$\phi = \frac{V_v}{V} \quad c = \frac{n_a}{V_f} = \frac{n_a}{V_v} = \frac{n_a}{\phi V} \quad \rho_s = \frac{n_s}{V_s} = \frac{n_s}{(1-\phi)\,V} \tag{2}$$

where n_a is the number of moles of acid and n_s the number of moles of calcium carbonate.

The governing laws of reactive flow within a volume V are the conservation of fluid mass

$$\frac{\partial \varphi}{\partial t} + u_{i,i} = 0 \tag{3}$$

conservation of acid molar mass

$$\frac{\partial (\phi c)}{\partial t} + (c u_i)_{,i} = \left(\phi D c_{,i}\right)_{,i} + R \tag{4}$$

and conservation of molar mass of the calcium carbonate

$$-\frac{\partial}{\partial t}\left(\frac{n_s}{V}\right) = -\frac{\partial}{\partial t}\left[\rho_s (1-\phi)\right] = \rho_s \frac{\partial \phi}{\partial t} = \frac{R}{2} \tag{5}$$

D is the diffusion coefficient with dimensions length squared over time. A comma denotes partial differentiation and the Einstein convention is used where repeated indices are summed. The fluid flux u_i is related to the pore pressure gradient through the constitutive equation of Darcy's law

$$u_i = -\kappa P_{,i} \tag{6}$$

where P is the fluid pressure and κ the permeability coefficient which can be expressed as k/μ where k is the intrinsic permeability $\left[\mathrm{m}^2\right]$ and μ the fluid viscosity [Pa s] and is assumed to be constant for simplicity. Although μ increases slightly with increasing acid concentration, the effect on κ is small compared to the effect of porosity change on k. The latter can be expressed by a porosity–permeability law like the Carman–Kozeny law

$$k(\varphi) = \frac{k_0 (1-\varphi_0)^2 \phi^3}{{\phi_0}^3 (1-\phi)^2} \tag{7}$$

where ϕ_0 and k_0 are the initial porosity and permeability, respectively. The porous rock due to dissolution is assumed to attain a maximum final porosity ϕ_f.

The advective–dispersive–reactive transport Eq. (4) contains a reaction term R which expresses the rate of loss of moles of acid per unit volume of rock and per unit time $\left[\mathrm{mol}/\left(\mathrm{m}^3\mathrm{t}\right)\right]$. The reaction term is also present in the conservation of molar mass of calcium carbonate Eq. (5) where the 1/2 coefficient results from the stoichiometry of the chemical reaction Eq. (1). Zhao et al.[8] and Chadam et al.[15] suggest a linear reaction rate term $R = r_0\left(\phi_f - \phi\right) c$ where r_0 is a reaction rate constant [1/s]. The reaction term is such that the reaction stops either when the concentration of the acid vanishes or when the porosity of rock reaches its maximum value so that all soluble solid has been dissolved. The explicit form of the reaction rate equation is not important in cases of high reaction rates where the thin front approximation is made because it assumes that the reaction is instantaneous.

The boundary value problem under consideration consists of a two-dimensional domain of infinite length ($-\infty < x < \infty$) and finite width W ($0 \le y \le W$), as shown in Fig. 3. An aqueous acid solution is injected at the inlet at prescribed constant molar acid concentration c_0 and fluid injection velocity u_0. The horizontal boundaries are no flux boundaries for both the molar acid concentration flux $c_{,y}$ and the fluid flux u_y. The initial conditions are everywhere at

$$t = 0: \qquad \phi = \phi_0, \quad c = 0 \tag{8}$$

and the boundary conditions are at

$$\begin{aligned} x \rightarrow -\infty: &\quad c = c_0, \qquad u_x = u_0 \\ x \rightarrow +\infty: &\quad c = 0 \\ y = 0, W: &\quad c_{,y} = P_{,y} = 0 \end{aligned} \tag{9}$$

From the fluid flux boundary condition, the pressure gradient at the inlet is

$$P_{,x}\big|_{x\rightarrow-\infty} = \delta_P = -\frac{u_0}{\kappa(\phi_0)} \tag{10}$$

As discussed earlier and well documented by Ladd and Szymczak,[18] in the limit of high reaction rates, reaction takes place only at a thin front separating the domain into a reacted region where rock has reached its maximum porosity and all

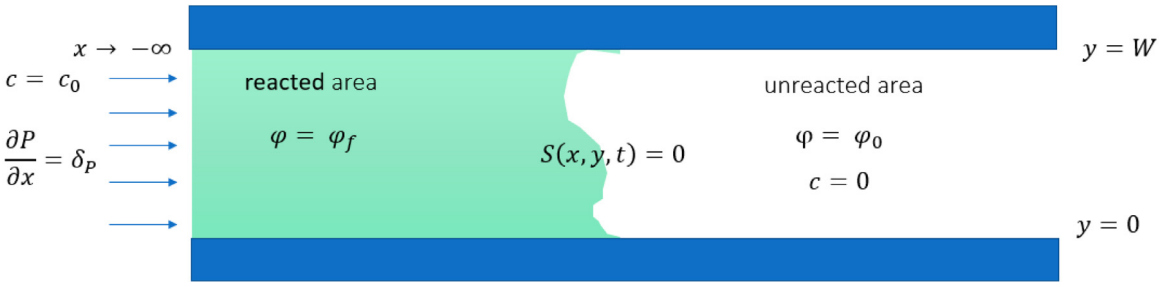

Fig. 3. Schematic of the domain and boundary conditions of the Stefan moving boundary problem for linear acidizing.

soluble solids have been dissolved and an intact region where rock is at its initial porosity. Since the reaction takes place only in a thin front, the rock can be either in the fully dissolved rock phase or the intact rock phase with the front separating these two phases of the Stefan problem. The front position becomes an unknown function $S\,(x, y, t)$ of space and time, while porosity can be either $\phi = \phi_f$ in the dissolved phase or $\phi = \phi_0$ in the intact phase. Under these considerations, the conservation Eqs. (3)–(5) of the general acid dissolution Stefan problem in Fig. 3 become in the reacted, dissolved phase behind the front at $S\,(x, y, t) < 0$

$$\begin{aligned} &u_{i,i} = 0, \qquad u_i = -\kappa\left(\phi_f, \mu_f\right) P_{,i} = -\kappa_f P_{,i} \\ &\phi_f \frac{\partial c}{\partial t} = \phi_f D c_{,ii} - (c u_i)_{,i} \end{aligned} \tag{11}$$

and in the unreacted, intact phase ahead of the front at $S\,(x, y, t) > 0$

$$\begin{aligned} &u'_{i,i} = 0, \qquad u'_i = -\kappa\,(\phi_0)\, P'_{,i} = -\kappa_0 P'_{,i} \\ &c = 0 \end{aligned} \tag{12}$$

Although fluid pressure can be described by a unique variable in both phases, it is chosen here, in order to simplify the mathematical treatment, to adopt two different dependent variables of pressure, i.e. P, P', for the two domains of the problem, the dissolved and the intact, respectively. Complementary to the two fluid pressures, two fluid fluxes u_i and u'_i are also introduced for the dissolved and intact phase, respectively. At the interface between the two phases, i.e. at the reaction front $S\,(x, y, t) = 0$, continuity equations are satisfied across the two phases for the fluid pressure and acid molar concentration

$$P = P', \qquad c = 0 \tag{13}$$

Moreover, conservation equations are satisfied across the front for the fluid mass and the acid molar mass. These are written, respectively, as

$$\left(u_i - u'_i\right) n_i = \left(\phi_f - \phi_0\right) V_i n_i \tag{14}$$

$$c_{,i} n_i = \frac{-2\rho_s\left(\phi_f - \phi_0\right)}{\phi_f D} V_i n_i \tag{15}$$

Eq. (14) expresses the jump of the fluid flux between the two phases as a result of the different porosities in each phase. This equation was derived using fluid mass conservation across the front, where V_i is the velocity of the moving front and n_i the unit normal to the front boundary, which is a line in two dimensions or a surface in three. Eq. (15) is derived from molar mass conservation across the front and it is called the Stefan condition. In addition to the above equations, the kinematic condition for the front

$$\frac{\partial S}{\partial t} + S_{,i} V_i = 0 \tag{16}$$

is necessary for the mathematical closure of the moving boundary problem.

4. Equilibrium state solution for uniform dissolution

The one-dimensional boundary value problem corresponding to uniform dissolution (equilibrium state) is shown in Fig. 4. Since there is no dependency on the y-axis, Eqs. (11)–(16) that describe the Stefan problem simplify as follows. The front position function is written as $S\,(x, y, t) = x - \zeta\,(t)$ while in the dissolved phase behind the front at $x < \zeta\,(t)$

$$u_{x,x} = 0 \quad \Rightarrow \quad P_{,xx} = 0, \qquad u_x = -\kappa_f P_{,x} \tag{17}$$

$$\phi_f \frac{\partial c}{\partial t} = \phi_f D c_{,xx} - u_x c_{,x} \tag{18}$$

and in the intact phase ahead of the front at $\zeta\,(t) < x$

$$\begin{aligned} &u'_{x,x} = 0 \quad \Rightarrow \quad P'_{,xx} = 0, \qquad u'_x = -\kappa_0 P'_{,x} \\ &c = 0 \end{aligned} \tag{19}$$

At the interface between the two phases, i.e. at the reaction front $\zeta\,(t) = x$, they simplify to

$$\begin{aligned} &P = P' \\ &c = 0 \\ &\lim_{x \to S(t)^-} u_x - \lim_{x \to S(t)^+} u'_x = \left(\phi_f - \phi_0\right) V_x = \left(\phi_f - \phi_0\right) \frac{d\zeta}{dt} \\ &c_{,x} = \frac{-2\rho_s\left(\phi_f - \phi_0\right)}{\phi_f D} V_x = \frac{-2\rho_s\left(\phi_f - \phi_0\right)}{\varphi_f D} \frac{d\zeta}{dt} \end{aligned} \tag{20}$$

where in the above, the kinematic condition for the front

$$\frac{\partial S}{\partial t} + S_{,x} V_x = 0 \quad \Rightarrow \quad -\frac{\partial \zeta}{\partial t} + V_x = 0 \quad \Rightarrow \quad V_x = \frac{\partial \zeta}{\partial t} \tag{21}$$

has been used to express the front velocity. The initial Eq. (8) and boundary conditions Eq. (9) apply. Wangen[21] proved that the right-hand side of the third of Eq. (20) is negligible since typically the front velocities are orders of magnitude smaller than the Darcy flow velocities. There appears to be a lack of a boundary condition for the downstream pressure P' to have closure in the mathematical problem but that does not affect the essential features of the problem since only the relative pressures and the pressure gradients are of interest.

In the solution of the partial differential equations, under the given the boundary conditions and the equation of interface motion for this Stefan problem, Lie group infinitesimal generators can be helpful. As discussed by Cherniha and Kovalenko,[22] for a Lie group to generate symmetries for a Stefan type moving boundary problem, all the variables and parameters of the problem, namely differential equations, boundary conditions and boundaries, should be left invariant under the action of the group, including the interface motion function $\zeta\,(t)$. Among all Lie groups that generate symmetries for the partial differential Eq. (18), the only one that leaves invariant all other equations is the generator $X = \partial_t + V_x \partial_x$. The front velocity V_x in this generator is a constant to be determined. Having found a Lie symmetry

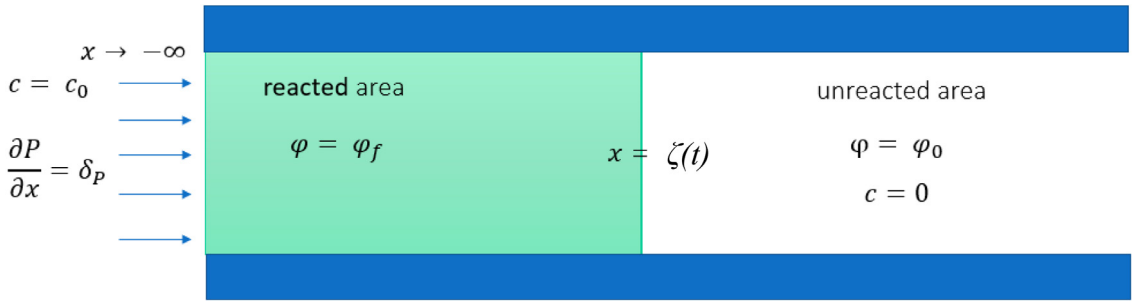

Fig. 4. Schematic of the domain and boundary conditions of the Stefan moving boundary problem for uniform dissolution (equilibrium state).

generator for the boundary value problem of interest, one can find a solution of the problem that is invariant under the action of the group. The solution invariant to the action of this generator is a traveling wave and is obtained by introducing the canonical coordinate ξ expressed as

$$\xi = x - V_x t \tag{22}$$

Applying the transformation Eq. (22), the second of the partial differential equations in Eq. (17) is transformed into the following ordinary differential equation

$$\frac{\partial^2 c}{\partial \xi^2} - A\frac{\partial c}{\partial \xi} = 0, \quad A = \frac{u_x/\phi_f - V_x}{D} > 0 \tag{23}$$

The solution of the Stefan problem is obtained by solving Eq. (23) and using the boundary and kinematic conditions. In the dissolved phase behind the front, i.e. for $\xi < 0$

$$P(\xi) = \delta_P \xi + P_0 \tag{24}$$

$$c(\xi) = c_0\left(1 - e^{A\xi}\right) \tag{25}$$

where $P_0 = P(\xi = 0)$ is the fluid pressure at the interface. In the intact phase ahead of the front at $\xi > 0$

$$\begin{aligned} &P'(\xi) = \overline{\kappa}\delta_P \xi + P_0, \quad \overline{\kappa} = \kappa_f/\kappa_0 \\ &c = 0 \end{aligned} \tag{26}$$

The interface velocity, which is constant in time, is given as

$$\frac{dS}{dt} = V_x = \frac{c_0 u_0/\phi_f}{c_0 + 2\rho_s\left(1 - \phi_0/\phi_f\right)} \tag{27}$$

It depends on acid injection rate, acid concentration and the difference between initial and final porosities. The parameter A must be larger than zero such that the solution of the Stefan problem satisfies the boundary conditions. This appears to be the case since the front velocity V_x is expected to be orders of magnitude smaller than the fluid interstitial velocity u_x/ϕ_f (cf. Eq. (23)). This agrees with the fast reaction assumption employed earlier which leads to the thin front approximation. The interface should advance sufficiently slow in order that enough acid enters and fully dissolves the calcium carbonate at each cross-section of the medium. Substitution of Eq. (27) in Eq. (23) for A and considering that in the dissolved area the fluid flux is constant and equal to u_0, yields

$$A = \frac{u_0/\phi_f - V_x}{D} = \frac{u_0/\phi_f}{D} \cdot \frac{2\rho_s\left(\phi_f - \phi_0\right)}{c_0 + 2\rho_s\left(1 - \phi_0/\phi_f\right)} \tag{28}$$

Eqs. (24)–(26) along with the front velocity Eq. (27) constitute the analytical solution of this Stefan moving boundary problem for which the equation of motion of the front is explicit and gives a unique solution. Eq. (24) shows that the pressure continuously decreases at a constant rate thus dictating a constant Darcy velocity in both reacted and unreacted domains. Eq. (25) shows that the acid concentration decreases exponentially while approaching the front. Fig. 5 plots a schematic of the fluid pressure, acid concentration and fluid flux profiles as a function of the coordinate ξ centered at the front. The pressure profile is plotted assuming that the pressure at the front is an arbitrary pressure P_0 that does not enter the problem since only the pore pressure difference is solved.

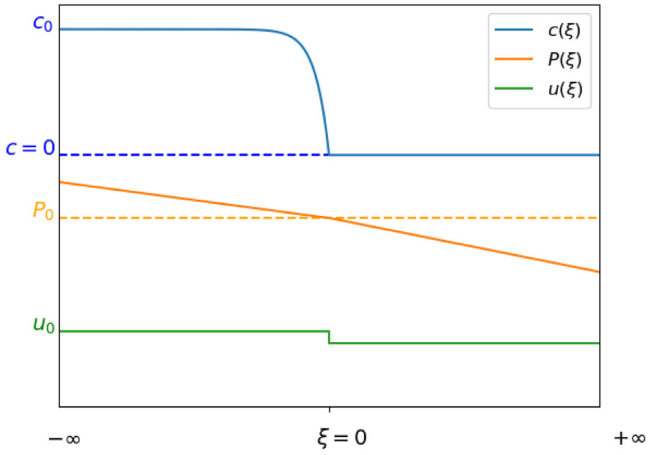

Fig. 5. Fluid pressure, acid concentration and fluid flux as a function of position in the equilibrium state solution.

Fig. 6 plots from Eq. (27) the front velocity V_x as a function of the fluid injection velocity u_0 and acid injection concentration c_0. The parameters used in these plots correspond to values used in the acidizing experiments in Mons chalk to be presented in Section 7. Typical HCl acid concentrations in applications are between 10%–30% v/v which correspond to $c_0 = 2.87$–9.45 mol/L. Fig. 6a shows the linear dependence of the front velocity on the fluid injection velocity. The results show that the front velocity is two orders of magnitude smaller than the fluid flow velocity. This slow movement of the front compared to the fluid velocity justifies the high reaction rate assumption and the thin front approximation which should not be violated by the results. Fig. 6b shows that the acid concentration affects in a parabolic way the front propagation velocity.

5. Scaling

Before proceeding to the scaling of the model it is useful to write the explicit equations of the general Stefan problem in two spatial dimensions by transforming Eqs. (11)–(16) from the $x-y-t$ system to the $\xi-y-t$ system. The position of the front is written as $S(\xi, y, t) = \xi - \zeta(y, t)$. Here the interface is not necessarily planar vertical, i.e. independent of y. Its form deviates from planar depending on the unknown function $\zeta(y, t)$. In this study, growth or decay of small disturbances from the planar

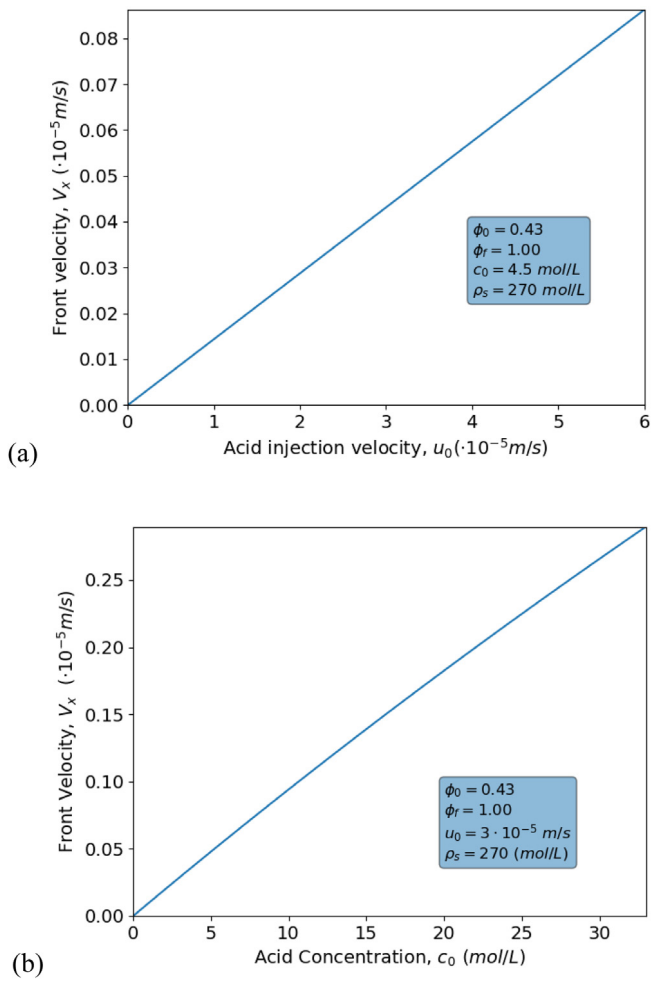

Fig. 6. Equilibrium state solution. Front velocity as a function of (a) fluid injection velocity and (b) acid concentration.

state are investigated and thus this function is assumed to take relatively small absolute values. In the dissolved phase behind the front, i.e. at $\xi - \zeta(y,t) < 0$

$$P_{,\xi\xi} + P_{,yy} = 0$$
$$\frac{\partial c}{\partial t} = V_x c_{,\xi} + D\left(c_{,\xi\xi} + c_{,yy}\right) + \frac{\kappa_f}{\phi_f}\left(c_{,\xi}P_{,\xi} + c_{,y}P_{,y}\right) \tag{29}$$

and in the unreacted, intact phase ahead of the front, i.e. at $\xi - \zeta(y,t) > 0$

$$P'_{,\xi\xi} + P'_{,yy} = 0$$
$$c = 0 \tag{30}$$

At the interface between the two phases, i.e. at the reaction front $\xi - \zeta(y,t) = 0$

$$P = P', \qquad c = 0$$
$$\overline{\kappa}\left(P_{,\xi} - \zeta_{,y}P_{,y}\right) = P'_{,\xi} - \zeta_{,y}P'_{,y}$$
$$c_{,\xi} - \zeta_{,y}c_{,y} = -\frac{2\rho_s\left(\phi_f - \phi_0\right)}{\phi_f D}\left(V_x + \frac{\partial \zeta}{\partial t}\right) \tag{31}$$

The process of scaling follows the guidelines set by Lin and Segel.[23] In their work, scaling amounts to non-dimensioning a model so that the intrinsic reference quantities give the order of magnitude of the corresponding variables in the phenomenon while the dimensionless variables exhibit an order of magnitude of unity. Since the dependent variables are functions of the equilibrium state solution, the intrinsic reference quantities can be extracted in a straightforward manner

$$c^* = c_0, \quad L^* = \frac{1}{A}, \quad t^* = \frac{1}{AV_x}, \quad P^* = -\frac{\delta_P}{A},$$
$$\zeta^* = \max|\zeta(y,t)| \tag{32}$$

Then the scaled variables become

$$\overline{c} = \frac{c}{c^*}, \quad \overline{\xi} = \frac{\xi}{L^*}, \quad \overline{y} = \frac{y}{L^*}, \quad \overline{t} = \frac{t}{t^*}, \quad \overline{P} = \frac{P}{P^*},$$
$$\overline{P'} = \frac{P'}{P^*}, \quad \overline{\zeta} = \frac{\zeta}{\zeta^*} \tag{33}$$

A small dimensionless parameter $\varepsilon = \zeta^*/L^*$ can be inserted in the equations because, as mentioned before, the deviations from planar state are small compared to the intrinsic length of the system. The parameters in Eq. (32) describe the intrinsic quantities of the system which express the order of magnitude of the corresponding variables. The non-dimensional variables in Eq. (33) have magnitude of order one as the scaling process dictates. Using Eqs. (32) and (33), the equilibrium state solution can be expressed in scaled variables. In the dissolved phase behind the front, i.e. at $\overline{\xi} < 0$

$$\overline{P} = -\overline{\xi} + \overline{P}_0$$
$$\overline{c} = 1 - e^{\overline{\xi}} \tag{34}$$

In the intact phase at $\overline{\xi} > 0$

$$\overline{P'} = -\overline{\kappa}\overline{\xi} + \overline{P}_0, \qquad \overline{P}_0 = -P_0 A/\delta_P$$
$$\overline{c} = 0 \tag{35}$$

The next step is to express the two-dimensional Stefan problem Eqs. (29)–(31) in the scaled variables. From this point forward, the dashes on the scaled variables are dropped for convenience. In the dissolved phase behind the front, i.e. at $\xi < \varepsilon\zeta$

$$P_{,\xi\xi} + P_{,yy} = 0$$
$$\frac{\partial c}{\partial t} = c_{,\xi} + \frac{1}{a_c}\left(c_{,\xi\xi} + c_{,yy}\right) + \left(1 + \frac{1}{a_c}\right)\left(c_{,\xi}P_{,\xi} + c_{,y}P_{,y}\right) \tag{36}$$

where

$$a_c = \frac{\phi_f c_0}{2\rho_s\left(\phi_f - \phi_0\right)} \tag{37}$$

In the intact phase at $\xi > \varepsilon\zeta$

$$P'_{,\xi\xi} + P'_{,yy} = 0$$
$$c = 0 \tag{38}$$

and at the interface $\xi = \varepsilon\zeta$

$$P = P', \qquad c = 0$$
$$\overline{\kappa}\left(P_{,\xi} - \varepsilon\zeta_{,y}P_{,y}\right) = P'_{,\xi} - \varepsilon\zeta_{,y}P'_{,y}$$
$$c_{,\xi} - \varepsilon\zeta_{,y}c_{,y} = -\left(1 + \varepsilon\frac{\partial \zeta}{\partial t}\right) \tag{39}$$

The scaling process reveals the existence of a dimensionless acid capacity number a_c in Eq. (37), which expresses the amount of acid needed to dissolve the available rock mass per unit volume of porous medium.

6. Linear stability analysis

The boundary value problem Eqs. (36)–(39) contains four unknowns, c, P, P' and the unknown interface shape function ζ. A linear stability analysis investigates the growth or decay of infinitesimal disturbances from the planar interface. This corresponds to seeking solutions to the vector problem $[\upsilon] = [\upsilon_b] +$

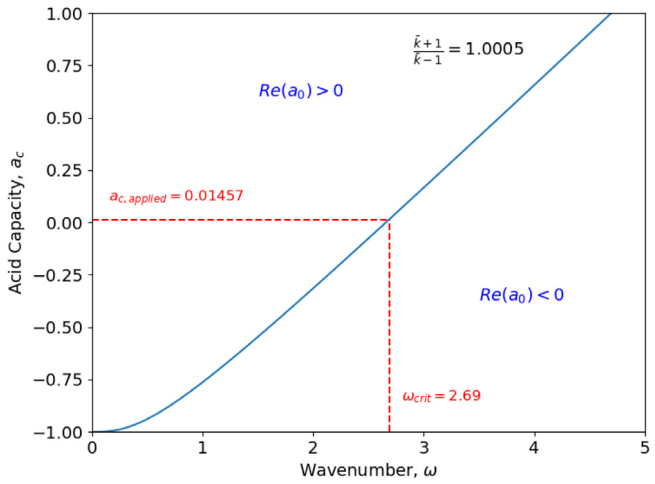

Fig. 7. Neutral stability line and regions of stability for the acid capacity number a_c vs. wavenumber ω depending on the sign of the Re (a_0).

$[\upsilon_1]$ where vector $[\upsilon_b]$ corresponds to the equilibrium state solution of the dependent variables and vector $[\upsilon_1]$ expresses sinusoidal disturbances with wavenumber ω and exponential growth coefficient α_0

$$[\upsilon] = \begin{bmatrix} c\,(\xi, y, t,\ \varepsilon) \\ P\,(\xi,\ y, t, \varepsilon) \\ P'\,(\xi,\ y, t, \varepsilon) \\ \varepsilon\zeta \end{bmatrix}, \qquad [\upsilon_b] = \begin{bmatrix} c_b\,(\xi) \\ P_b\,(\xi) \\ P'_b\,(\xi) \\ 0 \end{bmatrix},$$

$$[\upsilon_1] = \varepsilon \begin{bmatrix} c_1\,(\xi) \\ P_1\,(\xi) \\ P'_1\,(\xi) \\ \zeta_1 \end{bmatrix} \cos(\omega y)\, e^{a_0 t} \tag{40}$$

Introducing these specific solution forms into the boundary value problem allows the prediction of growth, decay or stability of each disturbance based on the sign of the real part of the eigenvalue a_0 in Eq. (40). The equilibrium solution $[\upsilon_b]$ satisfies the boundary conditions of the problem and therefore the instability solution $[\upsilon_1]$ satisfies homogeneous boundary conditions at the external boundaries, i.e.

$$\begin{aligned} &\xi \to\ -\infty, \quad c = c_b\,(\xi)\ , \quad P = P_b\,(\xi)\ , \quad c_1\,(\xi) = 0, \\ &P_1\,(\xi) = 0 \\ &\xi \to\ +\infty, \quad P' = P'_b\,(\xi)\ , \quad P'_1\,(\xi) = 0 \end{aligned} \tag{41}$$

Imposing the specific form of solution to the Stefan problem, expanding all terms in a Taylor series around $\varepsilon\zeta = 0$ and neglecting all terms of $O\left(\varepsilon^2\right)$ or higher, gives the following set of ordinary differential equations

$$\begin{aligned} &\frac{d^2 P_1}{d\xi^2} - \omega^2 P_1 = 0 \\ &\frac{d^2 c_1}{d\xi^2} - \frac{dc_1}{d\xi} - \left(\omega^2 + a_0\right) c_1 - (1 + a_c)\frac{dP_1}{d\xi} = 0 \\ &\frac{d^2 P'_1}{d\xi^2} - \omega^2 P'_1 = 0 \end{aligned} \tag{42}$$

with interface conditions

$$\begin{aligned} &(\bar{\kappa} - 1)\,\zeta_1 + P_1\,(0) - P'_1\,(0) = 0 \\ &c_1\,(0) - \zeta_1 = 0 \\ &\frac{dP_1\,(0)}{d\xi} - \frac{1}{\bar{\kappa}}\frac{dP'_1\,(0)}{d\xi} = 0 \\ &\frac{dc_1\,(0)}{d\xi} + a_0 - \zeta_1 = 0 \end{aligned} \tag{43}$$

Solving analytically the differential equations Eqs. (42) with the homogeneous boundary conditions Eqs. (41) gives the explicit expressions for $[\upsilon_1]$. Evaluating these expressions at the four interface conditions Eqs. (43) results in a homogeneous, linear, algebraic system of equations with coefficient matrix $[M]$

$$[M] = \begin{bmatrix} 0.5 + \sqrt{a_0 a_c + \omega^2 + 0.25} & -\dfrac{(1 + a_c)\,\omega^2}{a_0 a_c + \omega} & 0 & a_0 - 1 \\ 0 & 1 & -1 & \bar{\kappa} - 1 \\ 1 & -\dfrac{(1 + a_c)\,\omega}{a_0 a_c + \omega} & 0 & -1 \\ 0 & \omega & \omega/\bar{\kappa} & 0 \end{bmatrix} \tag{44}$$

For the homogeneous system to have a nontrivial solution, the determinant of $[M]$ must vanish. This results in an equation for the eigenvalue a_0

$$a_0 = 0.5 - g_1 + \frac{\bar{\kappa} - 1}{\bar{\kappa} + 1} \cdot \frac{(1 + a_c)\,(g_1 + \omega + 0.5)}{a_0 a_c + \omega} \tag{45}$$

where

$$g_1 = \sqrt{a_0 a_c + \omega^2 + 0.25} \tag{46}$$

Eq. (45) can predict the short-term fate of a disturbance expressed by the wavenumber ω relatively to the acid capacity number of the system. A similar calculation as in Wollkind and Segel[24] can prove the principle of exchange of stabilities for this system which means that a_0 has no pure imaginary roots, thus no oscillatory behavior is expected. This principle enables the investigation of the neutral stability conditions by setting $a_0 = 0$. The neutral line is then expressed by the following equation

$$a_c = \frac{\bar{\kappa} + 1}{\bar{\kappa} - 1} \cdot \frac{\omega\left(\sqrt{\omega^2 + 0.25} - 0.5\right)}{\sqrt{\omega^2 + 0.25} + \omega + 0.5} - 1 \tag{47}$$

Fig. 7 plots Eq. (47) and presents the results of the linear stability analysis where the neutral stability curve and the stable and unstable regimes are noted. The results are calculated for $\phi_0 = 0.43$ and $\phi_f = 0.97$ which give

$$\frac{\bar{\kappa} + 1}{\bar{\kappa} - 1} = \frac{(1 - \varphi_0)^2\,\phi_f^3 + \left(1 - \varphi_f\right)^2 \phi_0^3}{(1 - \varphi_0)^2\,\phi_f^3 - \left(1 - \varphi_f\right)^2 \phi_0^3} = 1.0005 \tag{48}$$

Points on the curve correspond to the zero value of growth factor a_0 and neutral stability where an infinitesimal disturbance from equilibrium will neither grow nor decay. The upper-left part of the plot is the unstable regime where the real part of growth factor is positive, i.e. Re $(a_0) > 0$, while the lower-right part is the stable regime with negative real part of growth factor, i.e. Re $(a_0) < 0$. For any acid capacity number there is a critical wavenumber ω_{cr} corresponding to neutral stability. All wavenumbers smaller than the critical belong to the unstable regime and all wavenumbers greater than the critical to the stable regime. From another point of view, for a specific wavenumber there is a critical acid capacity number above which infinitesimal disturbances grow and below which decay. By calculating for a specific acid capacity number, the growth factors a_0 for all wavenumbers smaller than the critical, it can be shown that the dominant wavenumber, i.e. the one with maximum growth rate a_0, is always the smallest one. The smallest wavenumber corresponds to the largest wavelength of the instability. The range of acid capacity number for injection of HCl acid solutions in calcite is $a_c = 0$ – 0.114. However, the plot in Fig. 7 is extended outside this range to better illustrate the form of the neutral stability line.

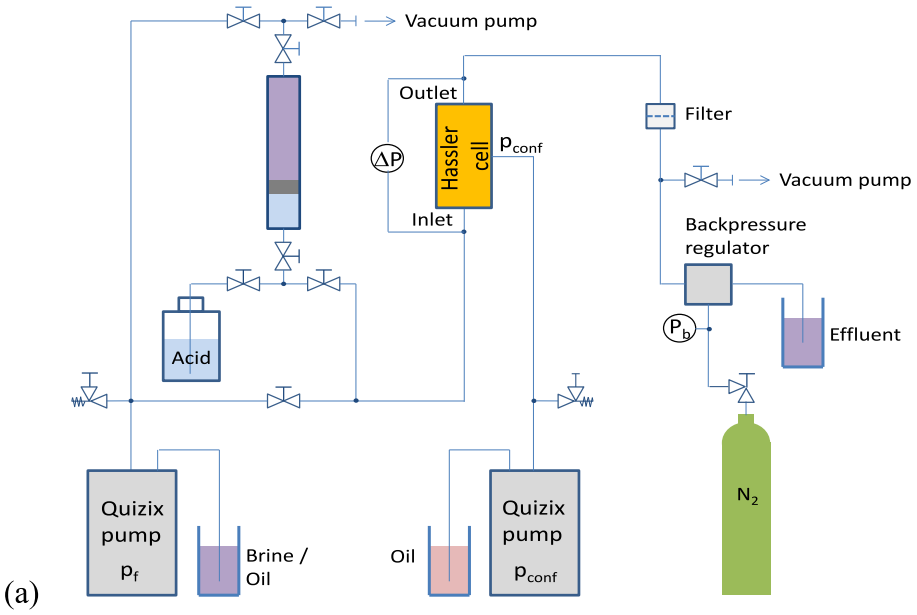

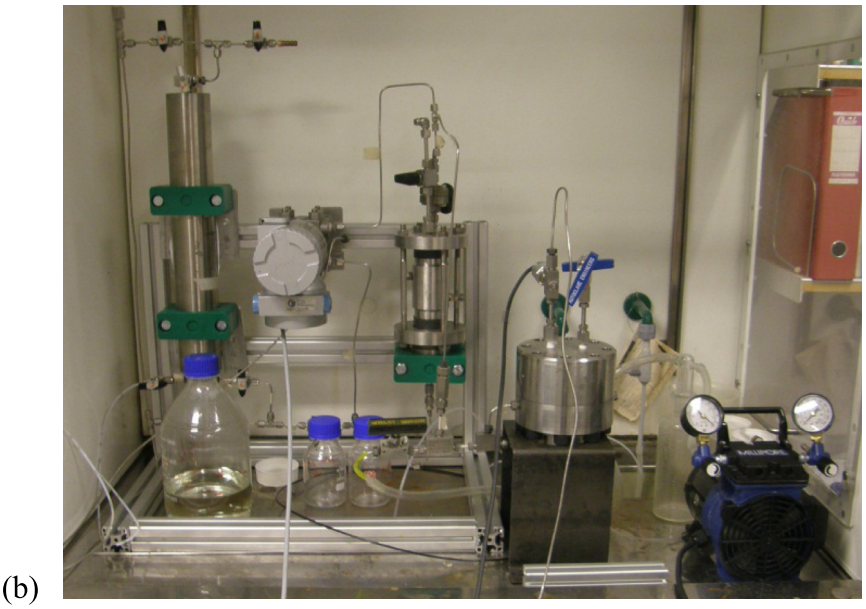

Fig. 8. (a) Schematic and (b) Photograph of the experimental setup for linear acidizing.

7. Acidizing experiments on chalk

Linear chalk acidizing was studied by injecting acid into cylindrical specimens of Mons chalk with diameter 3.8 cm and length 7.67 cm for a prescribed amount of time at a given rate. Mons has a porosity of ca. 42%–44% and a permeability of 2–3 mD. It has a been used as an analogue of high porosity North Sea chalk reservoirs. The specimens were initially either oil or brine saturated. An aqueous solution of hydrochloric acid (HCl) 15%v/v was used. The acidizing technique follows the procedure described by Izgec et al.[25] and Furui et al.[13] that studied acidizing of Kansas chalk. CT scans of the specimens were taken after acidizing. Fig. 8 shows a schematic and a photograph of the acidizing system. The chalk specimen is mounted in a Hassler cell that allows for fluid flow through the specimen and application of confining stress. The confining stress is applied only to the lateral side of the specimen. In the axial direction there is no stress actively applied to the end faces of the specimen. However, stress builds up in the axial direction as a reaction due to the Poisson's effect of the specimen since rigid caps are placed in contact with the specimen in that direction prohibiting any axial deformation. Acid was flowed axially through the specimen to create wormholes. The acid flow was stopped after wormhole breakthrough.

The fluid pressure difference over the specimen is measured by a differential pressure gauge. Fluid flow is controlled by a fluid pump, providing a constant flow rate, and a backpressure regulator. The backpressure, provided by a nitrogen pressure bottle, was set to 7 MPa ensuring that the CO_2 generated during acidizing stays dissolved in the liquid. The confining stress was set to values between 9 and 9.5 MPa, allowing for fluid pressure differences 2–2.5 MPa over the specimen. The fluid pump that controls the fluid flow is connected to both the Hassler cell and an acid filled accumulator. As shown in Fig. 8a, the flow loop is set up in such a way that either saturation fluid or acid is flowed through the specimen. The saturation fluid was oil (kerosene) or brine (Ekofisk field simulated brine; salt content ≈ 7 wt%).

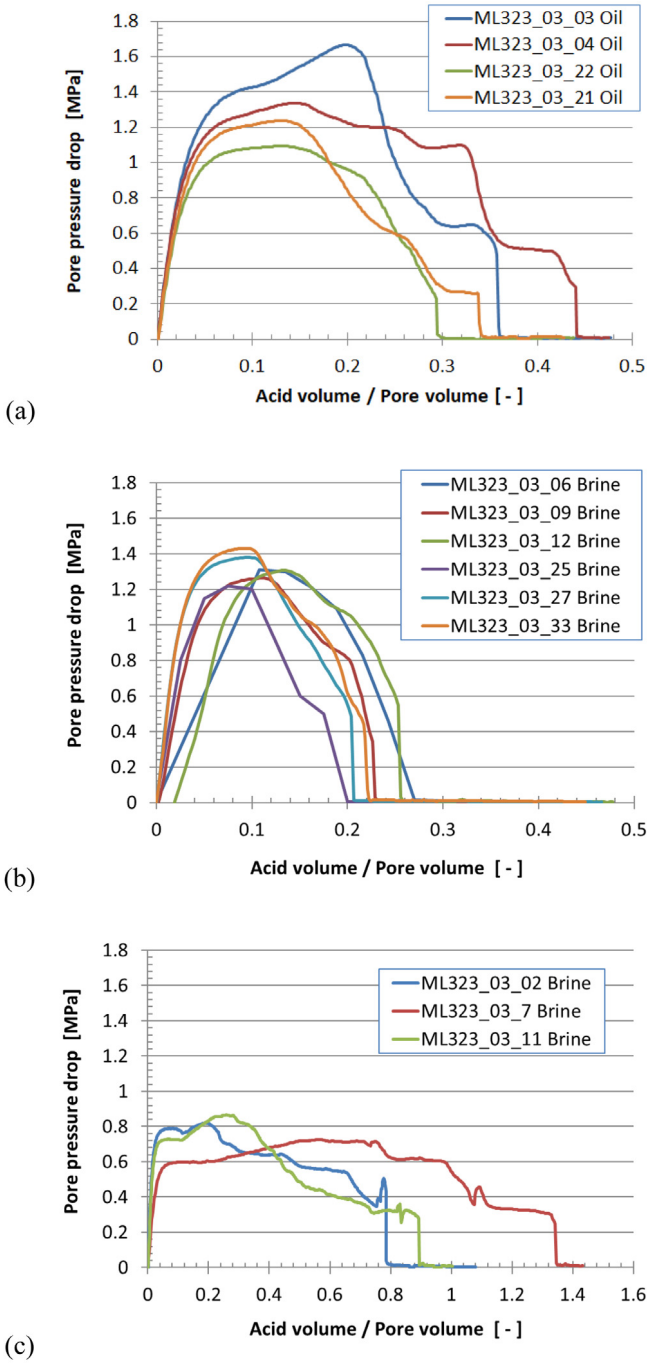

Fig. 9. Pore pressure drop vs. injected acid volume over specimen pore volume for Mons chalk acidizing tests on (a) oil saturated specimens at 0.022 mm/s acid injection velocity and brine saturated specimens at (b) 0.044 mm/s and (c) 0.022 mm/s acid injection velocity.

The chalk specimens were oven dried at 80 °C for more than 48 h and subsequently vacuum saturated with oil or brine in the Hassler cell. Before placement in the Hassler cell, the specimens were wrapped with two rounds of Teflon tape including the porous platens at each end and then they were surrounded with a Viton sleeve. The Teflon was used to protect the sleeve from the corrosive action of HCl. Flowing was continued for about 1 Pore Volume (PV) of saturation fluid through the specimen before switching to acid flow. Flow rates were set to 1.5 mL/min for oil saturated specimens and 3 mL/min for brine saturated specimens.

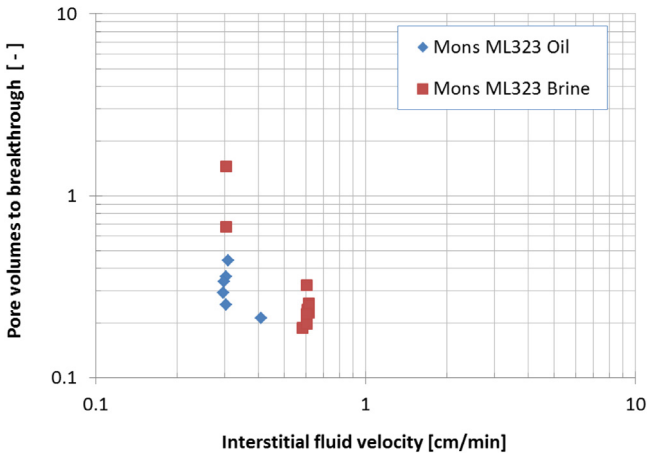

Fig. 10. Amount of acid flowed through cylindrical chalk specimens until wormhole breakthrough (PVTB) vs. interstitial fluid velocity for oil and brine saturated Mons chalk.

Some other flow rates were also tried, like e.g. 1.5 mL/min for brine saturated specimens, but the selected ones gave the best results with respect to wormhole formation. The selected flow rates were high enough to result in wormholes that do not intersect the side of the specimen but low enough to keep the pressure drop over the specimen below 2 MPa, otherwise the confining stress would have to be increased with the risk of damaging the rock. The 1.5 and 3 mL/min correspond to fluid injection velocities (=flow rate/cross-sectional area) of 0.022 and 0.044 mm/s and interstitial fluid injection velocities (=fluid velocity/porosity) of 0.0505 and 0.101 mm/s. Not all tests gave breakthrough wormholes, and this was the case especially for the tests run at not optimum flow rates. The specimen porosity ϕ was obtained from the specimen dry weight w_d and volume V as $\phi = 1 - w_d/\rho_s V$, where the density of calcite $\rho_s = 2710$ kg/m^3 was used for the solids.

The pressure difference over the specimen decreased during acidizing with a sharp drop to zero upon wormhole breakthrough. Shortly after wormhole breakthrough the acid flow was stopped and about 1 PV of saturation fluid, i.e. oil or brine, was flowed through the specimen to stop the acidizing process. The fluid pressure and confining stress were then released, and the specimen was dismounted. Fig. 9 presents the experimental results for oil saturated specimens with acid injection rate 1.5 mL/min and for brine saturated specimens with injection rate 3.0 mL/min and 1.5 mL/min. The results show good repeatability at all conditions. Table 1 summarizes the important parameters for each saturation fluid and injection velocity. Average values for each condition are listed.

Successful wormholing is characterized by the development of a wormhole with the lowest possible consumption of acid. The results show that this is achieved by applying similar pore pressure gradients (and pore pressure drops for the same length specimens) which are around 18 MPa/m. Thus, a higher flow velocity of 0.044 mm/s is necessary in the brine saturated specimens than the 0.022 mm/s velocity in the oil saturated specimens. Similar PVTBs are obtained in both cases. On the other hand, for flow velocity 0.022 mm/s in the brine saturated specimens (Fig. 9c), suboptimum wormholing is obtained with 4–5 times larger consumption of acid than for the 0.044 mm/s flow velocity.

About 0.2–0.5 PV of acid were needed until wormhole breakthrough. Fig. 10 shows a plot of the PVTB as a function of interstitial fluid velocity. The results show a relatively good repeatability for velocities 0.3 cm/min (flow rate 1.5 mL/min) for oil and

Table 1
Summary of acidizing test results on cylindrical specimens of oil and brine saturated Mons chalk.

Dry density [g/cm^3]	ϕ [%]	Saturation fluid	Fluid injection rate [mL/min]	Fluid velocity [mm/s]	Interstitial fluid velocity [mm/s]	Max pore pressure gradient [MPa/m]	Pore Volume To Breakthrough [–]
1.536	43.3	Oil	1.5	0.022	0.051	17.3	0.337
			2.0	0.029	0.068	21.9	0.212
		Brine	1.5	0.022	0.051	10.5	0.974
			3.0	0.044	0.101	18.7	0.240

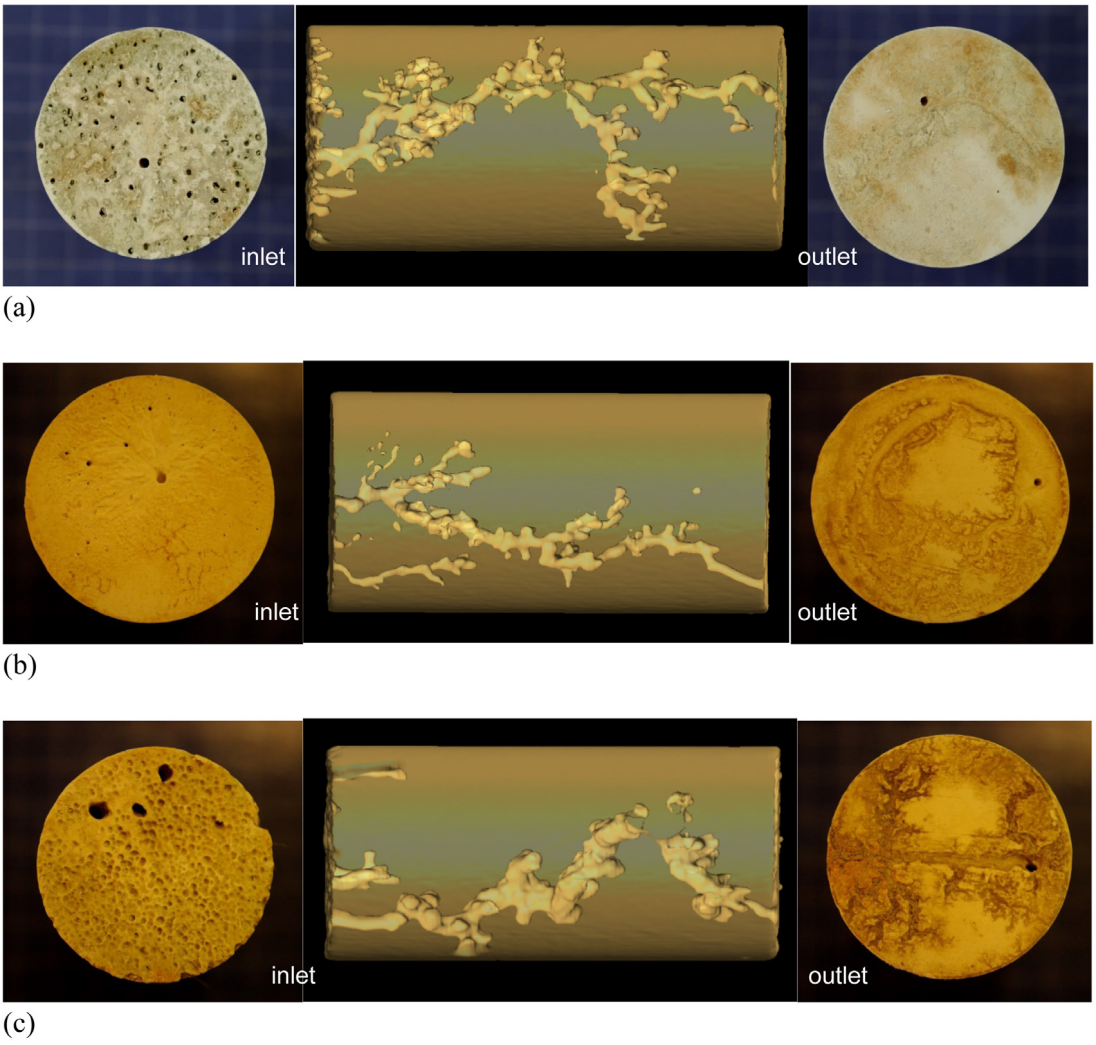

Fig. 11. Representative photographs of inlet face (left), CT-scan-based 3D reconstruction of wormholes (middle) and outlet face (right) of (a) an oil-saturated specimen acidized at 1.5 mL/min (ML323_03_04), (b) a brine-saturated specimen acidized at 3 mL/min (ML323_03_12), and (c) a brine-saturated specimen acidized at 1.5 mL/min (ML323_03_12). Test names refer to the names in the legends in Fig. 9.

0.6 cm/min (flow rate 3 mL/min) for brine saturated specimens, respectively. The results are in qualitative agreement with results obtained by Furui et al.[13] in a systematic study where acid volumes to breakthrough were measured for 25.4 mm diameter and 101.6 mm diameter Kansas chalk cylinders for various interstitial fluid velocities and different acid concentrations and temperatures. The Kansas chalk they used had porosity around 32%. A comparison shows that breakthrough volumes are similar for Mons and Kansas chalk for comparable interstitial fluid velocities.

Fig. 11 shows representative photographs of acidized oil and brine saturated chalk specimens together with a 3D visualization of the wormholes reconstructed from CT images. The acid was flowed from left to right. The exit holes on the outlet faces are clearly visible. As observed in previous studies (McDuff,[2] Furui et al.[13]), the wormholes have rather complex structure and exhibit several branches. Some of the branches intersect the side of the specimens as e.g. in Fig. 11c. The diameter of the wormholes in Fig. 11a,b are in the order of 1 mm while in Fig. 11c is in the order of 2 mm. When the flow rate is lower that the optimum rate then the wormholes become larger and more acid is required for their development.

7.1. Local strength mapping near the wormholes

The local strength variations from wormhole to intact rock in the acidized chalk specimens were investigated in one oil and one brine saturated specimen. The objective was to find the spatial effect of the acid action on the chalk strength and whether an area of reduce strength surrounds the wormholes. This would

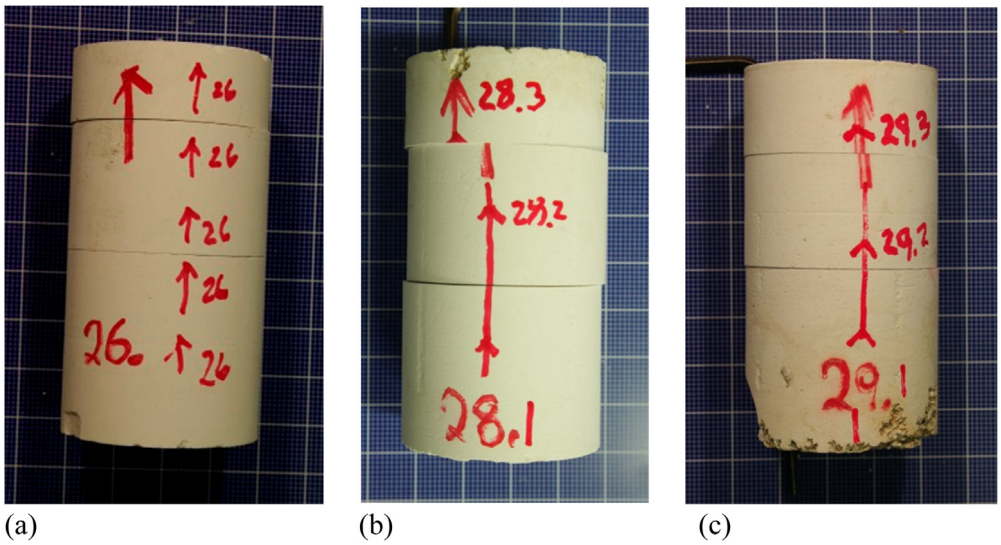

Fig. 12. Photographs of the specimens tested with the durometer: (a) Reference specimen of virgin chalk (ML323_03_26), (b) Acidized oil saturated specimen (ML323_03_28), and (c) Acidized brine saturated specimen (ML323_03_29).

verify experimentally the thin front assumption made in the development of the theoretical model of chemical dissolution.

The strength mapping was made using a durometer. Durometer is one of several measures of hardness of a material which may be defined as a material's resistance to permanent indentation. The durometer scale was defined by Shore[26] who developed a measurement device to measure the Shore hardness in the 1920s. Shore's device was not the first hardness tester nor the first to be called a durometer but today that name usually refers to Shore hardness (other devices are simply called hardness testers). Hardness measurements have been related to stiffness and strength and therefore the durometer is considered as a convenient way to identify potential variations in mechanical properties around the wormholes. There are several durometer scales used for materials with different properties. In our case the ASTM D2240 type D scale was used. The Type D scale uses a hardened steel rod 1.4 mm diameter with a 30° conical pin and 0.1 mm radius tip. It has a 2.54 mm travel and can measure a force up to 44.42 N. The principle used to measure hardness is based on measuring the resistance force of the penetration of a pin into the test material under a known spring load. The amount of penetration or resistance force is converted to hardness reading on a scale with 100 units.

The procedure of the durometer test is to first place the specimen on a hard, flat surface. The indenter for the instrument is then pressed into the specimen making sure that it is parallel to the surface. Once the gauge is pressed firmly against the material and the needle has penetrated as far as it can go, the measurement needle will indicate the corresponding hardness measurement. The test specimens are generally 6.4 mm thick. It is possible to pile several specimens to achieve the 6.4 mm thickness, but one specimen is preferred. It is recommended to test at least 12 mm from any edge and perform five tests at least 6.35 mm apart and use the average value.

Cross sectional cuts of the tested specimens were made to obtain specimens to test with the durometer. Fig. 12 shows photographs of the tested specimens and the location of the cuts. Besides the acidized oil and brine saturated specimens, a virgin specimen was also tested for reference. All specimens were oven dried at 90 °C for at least 24 h prior to testing with the durometer. Fig. 13 shows the location of the indentation measurements. Table 2 lists the measurements which had good repeatability. The average hardness of the reference virgin chalk is 69.6. In the acidized specimens the reference values far from the wormhole, i.e. at a distance > 8 mm, are 63.4 and 64.1 for the oil and brine saturated specimen, respectively. Closer to the wormhole at distances 1.5–8 mm the hardness values are close to the reference, except in the cases where the indentation tip collapsed into the wormhole resulting in much lower values than the reference.

The results show that the acidized specimens are slightly weaker than the reference specimen. However, since the porosity of the reference specimen was not obtained, the difference may result from specimen variation given also the fact that the porosities of the acidized specimens are larger than 44% which is in the high side of porosity for the tested block of Mons (cf. average porosity 43.3% in Table 1). There seems to be no effect of the saturation fluid, i.e. oil or brine during acidizing since the specimens were oven dried after acidizing. Also there seems to be no significant difference between far from the wormhole and close to the wormhole except for the cases where the indentation tip collapsed into the wormhole. Thus, the acid affected zone around the wormhole does not extent more than 1.5 mm and it may be smaller than that. This is also corroborated from the CT scans that do not show any area of reduced density near the wormholes.

8. Analysis of experimental results

In the following the experimental results are analyzed within the framework of the developed model that views wormholes as the result of reactive instabilities. An acid concentration of 15% v/v or $c_0 = 4.5$ mol/L injected in calcite of $\rho_s = 270$ mol/L with initial porosity $\phi_0 = 0.43$ and final porosity $\phi_f = 1$ results in an acid capacity number $a_c = 0.01457$. For these conditions the critical wavenumber is $\omega_{cr} = 2.69$, as depicted with the dashed red lines in the plot in Fig. 7. This is a general observation which uses the main dispersion relation Eq. (45) of the scaled non-dimensional model. This means that all instabilities with wavenumber $\omega \leq \omega_{cr}$ will grow. To study the actual wavelengths and critical values of the various parameters one must use the intrinsic scales of the system expressed during the scaling process. The actual wavelength λ of the perturbation is calculated by multiplying the dimensionless wavelength $\bar{\lambda} = 2\pi/\omega$ with the intrinsic length L^* of the system to obtain the wavelength to

Table 2
Durometer hardness measurements on reference Mons and acidized Mons specimens far and close to the wormhole.

Saturation fluid during acidizing	ϕ [%]	Distance from wormhole	Hardness							Average hardness
Reference ML323_03–26	–	–	71	67.5	69	71.5	73	67	68	69.6
Oil ML323_03_28	44.1	>8 mm	65.5	62.5	63.5	63	62.5			63.4
		1.5–8 mm	65.5	64						64.8
		1.5–2 mm + collapse into wormhole	25	30	22					25.7
Brine ML323_03_29	44.4	>8 mm	64	67	65	63.5	66			64.1
		1.5–8 mm	62	62	63	61				62.0
		1.5–2 mm + collapse into wormhole	25							25.0

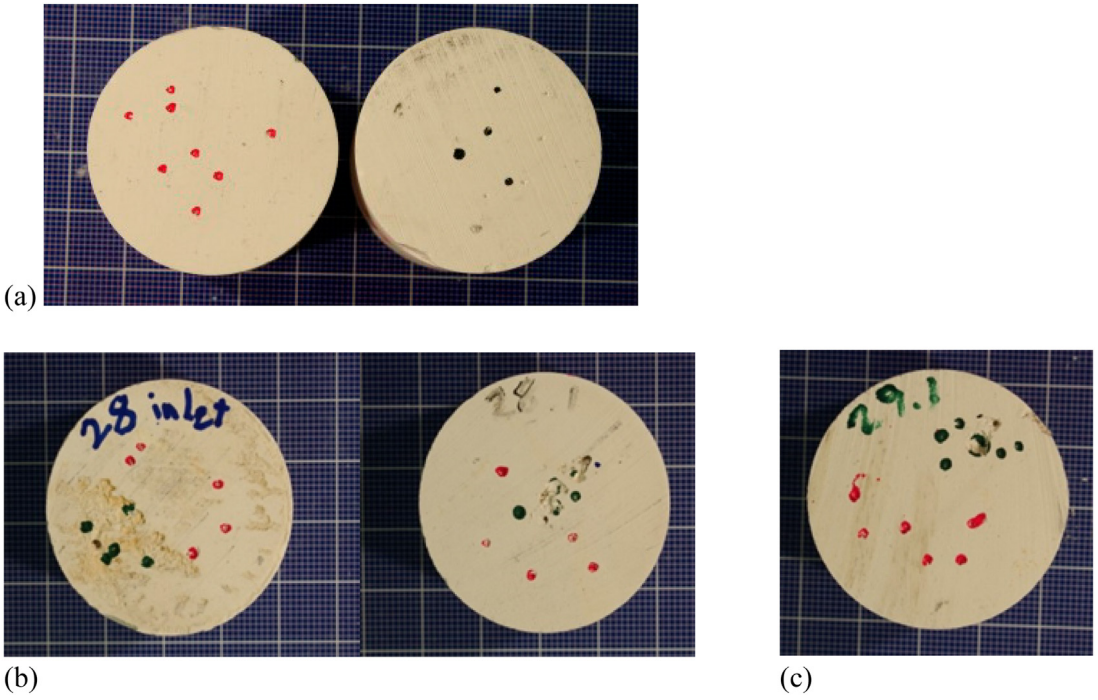

Fig. 13. Location of the indentation tests in (a) Reference virgin specimen (ML323_03_26), (b) Acidized oil saturated specimen (ML323_03_28) (left, inlet surface; right, inside surface), and (c) Acidized brine saturated specimen (ML323_03_29) (inside surface). Specimen diameter is 38 mm.

wavenumber relation

$$\lambda = \frac{2\pi}{\omega} L^* \tag{49}$$

The intrinsic length L^* is defined through Eqs. (28) and (32) and depends on the diffusion–dispersion coefficient D, the acid injection velocity u_0 or equivalently the imposed pressure gradient δ_P at the inlet of the system and the front velocity V_x which is known from the equilibrium state solution Eq. (27). However, the contribution of the front velocity in the calculation of intrinsic length L^* can be neglected since it is two orders of magnitude less than the fluid flux or alternatively the mol concentration of acid c_0 is two orders of magnitude less than the calcite mol density ρ_s, i.e.

$$L^* = \frac{D}{u_0/\phi_f - V_x} = \frac{D}{u_0/\phi_f} \cdot \left[1 + \frac{c_0}{2\rho_s\left(1 - \phi_0/\phi_f\right)}\right] \approx \frac{D}{u_0} \tag{50}$$

The critical wavenumber corresponds to different critical wavelengths depending on the ratio u_0/D of fluid velocity to diffusion–dispersion coefficient. This ratio expresses the opposing roles of advection and diffusion in amplifying or decaying respectively the infinitesimal disturbances from equilibrium in reactive infiltration. In the limit of infinite pressure gradient or fluid velocity (or equivalently in the limit of zero diffusion–dispersion coefficient) the ratio $u_0/D \to \infty$ and the intrinsic length $L^* \to 0$. This causes the actual critical wavelength to tend to zero and any disturbance will grow. This is reasonable since the destabilizing processes dominate over the stabilizing ones. Conversely in the absence of advection (or equivalently in the limit of infinite diffusion–dispersion coefficient) the ratio $u_0/D \to 0$ and the critical wavelength tends to infinity thus causing perturbations of any size to decay.

As mentioned earlier, for a specific acid capacity number the dominant wavenumber is the smallest of all wavenumbers to the left of the critical one in the horizontal axis of Fig. 7, which is reproduced in Fig. 14 for realistic values of acid capacity number for HCl acid injection in Mons chalk. When applying these results to a physical model as in the experiments, there is the restriction of the width W of the system. The actual wavelength λ of the instability relates to the width W through the expression $\lambda = 2\,W/n$, where $n = 1, 2, 3, \ldots$, such that the boundary conditions at the upper and lower boundary are satisfied for the perturbation solution $[\upsilon_1]$ in Eq. (40) and the sinusoidal disturbance has sufficient width to develop. Fig. 15 shows the waveforms of the five larger wavelengths that correspond to $n = 1, 2, 3, 4, 5$ and develop in a medium of width W.

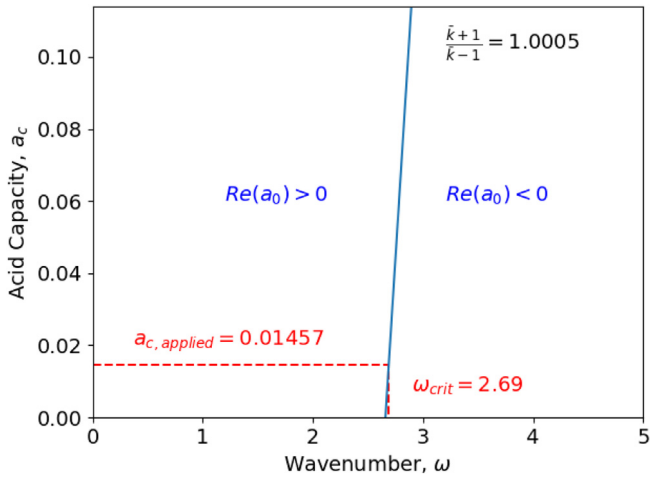

Fig. 14. Neutral stability line and regions of stability for the acid capacity number a_c vs. wavenumber ω depending on the sign of the Re (a_0).

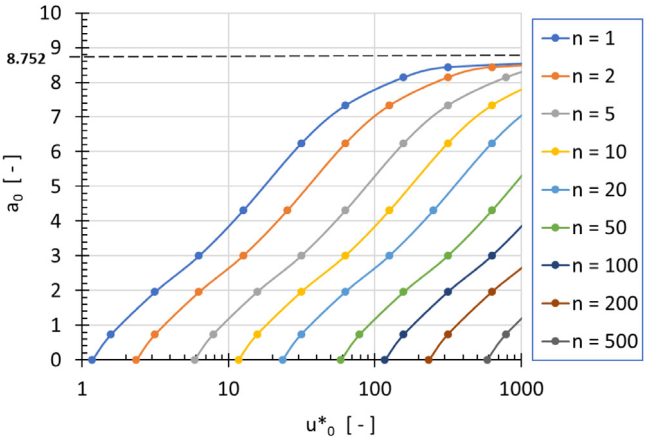

Fig. 16. Growth rate a_0 as a function of dimensionless injection fluid velocity u_0^* for various n values of the wavelength of the instability.

Substitution in Eq. (49) and use of Eq. (50) gives the wavenumber ω as a function of intrinsic length L^* and dimensionless injection velocity u_0^*

$$\omega = \frac{n\pi}{W}L^* = \frac{n\pi}{u_0^*}, \qquad u_0^* = \frac{Wu_0}{D} \tag{51}$$

The solution of the implicit nonlinear Eq. (45) renders the growth rate a_0 for every wavenumber ω. Combining this result with Eq. (51), the growth rate a_0 can be calculated for a given value of n and u_0^*. Fig. 16 plots the growth rate a_0 as a function of the dimensionless injection fluid velocity u_0^* for various n or equivalently wavelengths λ of the instability. The results show that instabilities with positive growth rate are possible for injection velocities $u_0^* > 1.168$. This injection velocity gives the instability with $n = 1$ and larger wavelength $\lambda = 2W$. At higher injection velocities, instabilities with smaller wavelengths (larger n) are possible. For example, for $u_0^* = 11.68$, all instabilities with $n =$ 1–10 have positive growth rate. However, from all the different wavelengths the largest wavelength for $n = 1$ has the largest growth rate. The growth rate has an asymptote for $\omega \to 0$ which for the particular problem is $a_0^{\max} = 8.752$ as marked in Fig. 16.

These findings are in accordance with experimental results[2,3] that show that a primary wormhole (instability) develops at a given injection fluid velocity while at higher velocities besides the primary wormhole, secondary wormholes develop also resulting in a dendritic, ramified network. The density of this network increases with increasing injection velocity because more instabilities of smaller wavelength have now positive growth rate. This means that for an optimum acidizing process with minimum amount of acid spent and a single wormhole, the optimum injection fluid velocity will be the smallest one with positive growth rate. It will have the largest possible wavelength. For the parameters at hand, the optimum dimensionless injection velocity $u_{0\_opt}^* = \pi/\omega_{cr} = 1.168$. Fig. 17 plots $u_{0\_opt}^*$ vs. the acid capacity number a_c. using the results from Fig. 14. The values of a_c in the plot correspond to the injection of HCl acid with concentrations 0 to 100% v/v in Mons chalk. Thus, for a given HCl concentration the optimum injection velocity can be obtained.

Eq. (51) gives a scale effect with respect to the width W of the model for the dimensional optimum injection velocity u_{0_opt}

$$u_{0\_opt} = \frac{u_{0\_opt}^* D}{W} = \frac{\pi D}{\omega_{cr} W} \tag{52}$$

Thus, the optimum injection velocity scales with the inverse of the model width. This theoretical result is in accordance with scaled experiments performed by Furui et al.[13] who tested samples of different widths and showed the same scaling of optimum acid injection velocity to sample width.

The previous analysis can be applied to the acidizing experiments in Section 7 and the results can be compared with the experimental measurements. The width of the system is taken equal to the diameter of the specimen, i.e. $W = 0.038$ m. This approximation neglects the difference in geometry between the theoretical model that has an infinite depth and the specimen that has a cylindrical geometry. The optimum dimensional injection velocity u_{0_opt} for the experimental setup can be predicted using Eq. (52) provided that the diffusion–dispersion coefficient D is known. This coefficient is written as $D = D_F + D_S$ where D_F is the molecular diffusion part and D_S the dispersivity associated with hydrodynamic dispersion.[27] Molecular diffusion for relatively high flow velocities like this one is three to four orders

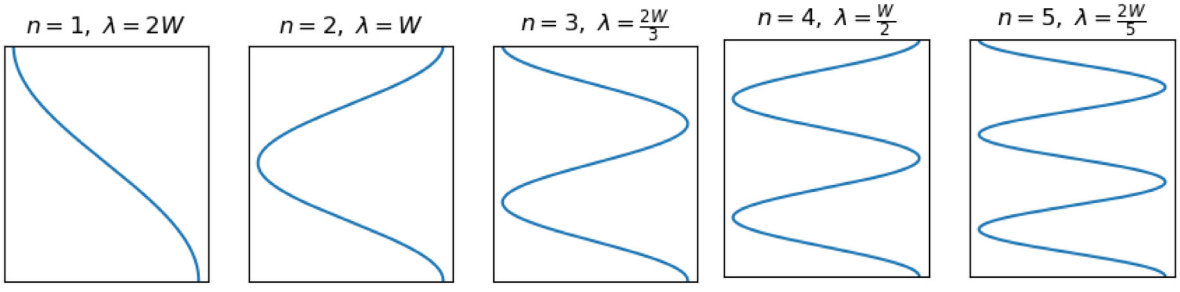

Fig. 15. Waveforms of the instabilities with the five larger wavelengths λ for $n = 1, 2, 3, 4, 5$ that develop in a medium of width W.

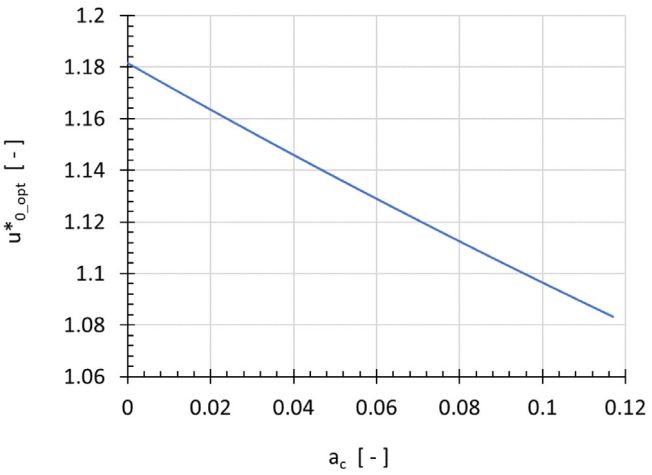

Fig. 17. Optimum dimensionless injection fluid velocity $u^*_{0\_opt}$ as a function of acid capacity number a_c for various HCl injection concentrations and Mons chalk.

of magnitude less than the hydrodynamic dispersion and therefore D_F can be neglected. The hydrodynamic dispersivity D_S is assumed to be linearly dependent on fluid velocity, i.e. $D \simeq D_S = a_L u/\phi$, where a_L is the longitudinal diffusivity with dimension length. Although no measured values of a_L for flow of HCl solution in Mons chalk were found in the literature, Schulze-Makuch[28] report a value of $a_L = 1$ m for chalk which when scaled from 8 m to the 0.08 m length of the laboratory specimen, using the proposed square root scaling law, gives a value of $a_L = 0.1$ m. Furthermore, Mathias[29] in his numerical simulations in chalk aquifers used $a_L = 0.04$ m for chalk. These values of a_L and the fluid velocity of the experiments listed in Table 1 for brine, yield $D = a_L u/\phi = 0.04{-}0.1{\cdot}0.044{\times}10^{-3}/0.433 = 4{-}10{\times}10^{-6}$ m^2/s. In our case, a value of $a_L = 0.01$ m giving $D = 1{\times}10^{-6}$ m^2/s, yields an optimum fluid injection velocity and pressure gradient at inlet that compares well with the experimental results in Table 1

$$u_{0\_opt} = \frac{u^*_{0\_opt} D}{W} = \frac{\pi D}{\omega_{cr} W} = \frac{1.168 \cdot 1 \cdot 10^{-6}}{3.8 \cdot 10^{-2}} = 3.05 \cdot 10^{-5} \text{ m/s}$$
$$u_{0\_opt} = \frac{k_0}{\mu}\delta_p \Rightarrow \delta_P = \frac{\mu u_{0\_opt}}{k_0} = \frac{1.2 \cdot 10^{-9} \cdot 3.05 \cdot 10^{-5}}{2 \cdot 10^{-15}} = 18.6 \text{ MPa/m} \quad (53)$$

where a chalk permeability of 2 mD and a constant viscosity for the HCl solution of 1.2 cP were used.

9. Conclusions

Reactive instabilities developing during linear acidizing in pure calcite chalks were studied. First the equilibrium state, uniform front solution was analyzed within a moving boundary value problem formulation in an infinite domain. This analysis results in a self-similar problem that spatially depends only on the distance from the location of the front as the front travels through the medium at constant velocity. The solution assumes a thin dissolution front where all reaction takes place and allows the separation of the domain into two distinct regions, the fully reacted region behind the front and the unreacted region ahead of the front. This assumption is validated by experiments that did not indicate the existence of a transition zone between reacted and unreacted region.

The analytical solution for the equilibrium state was combined with a linear stability analysis which investigated whether additional infinitesimal sinusoidal solutions or perturbations have positive growth rates. The growth of these reactive instabilities is presumed to lead to the formation of wormholes in linear acidizing experiments. The stability analysis shows that for a given acid capacity number, i.e. formation and injection acid concentration, there is a critical wavenumber below which all instabilities grow at an increasing rate as the wavenumber decreases. When applying the results to the physical model of linear acidizing experiments, the restriction of the width of the system relates the wavelength of the instability to the width. This results in an optimum injection velocity for the growth of an instability with wavelength twice the specimen width which grows to a single wormhole. Above the optimum injection velocity, instabilities with smaller wavelengths also grow resulting in a ramified, dendritic network of wormholes as observed in experiments. The analysis shows that the optimum injection velocity scales with the inverse of the specimen width as also observed in experiments and reported in the literature.

A set of linear acidizing experiments on Mons chalk specimens was performed to compare the modeling results with experimental measurements. A 15% v/v hydrochloric acid solution was injected in cylindrical specimens at different injection velocities and the optimum injection velocity for wormhole formation was obtained. The quantitative comparison of the optimum injection velocity from the model and the acidizing experiments, requires a value for the diffusion–dispersion coefficient for HCl flow in Mons. Alternatively, this coefficient can be back calibrated from the experimental results. The obtained value in this case appears to be smaller by a factor 4 to 10 as compared to values for chalk aquifers obtained from the literature. However, the range of values of these coefficients is rather wide and it may include scale effects and/or other measurement artifacts. This suggests that back calibration from experiments for a particular problem is a reasonable alternative. In field applications, field calibration can be performed instead.

Declaration of competing interest

The authors declare that they have no known competing financial interests or personal relationships that could have appeared to influence the work reported in this paper.

Acknowledgments

The authors would like to thank Lars Erik Walle and Eyvind Sanstebø for their contribution in the experimental part of this work which was carried out with the financial support of Aker BP, ConocoPhillips Norway, Hess Denmarkwithin the Joint Industry Project ‘Chalk influx in production wells’.

References

1. Economides MJ, Hill AD, Economides-Ehlig C, Zhu D. *Petroleum Production Systems*. 2nd ed., Prentice-Hall: Westford; 2013, p. 622.
2. McDuff DR, Shuchart CE, Jackson SK, Postl D, Brown JS. Understanding wormholes in carbonates: Unprecedented experimental scale and 3D visualization. In: *SPE134379, Proc. SPE Annual Technical Conference and Exhibition 2010*. Florence, Italy.
3. Fredd CN, Fogler HS. Alternative stimulation fluids and their impact on carbonate acidizing. *Soc Pet Eng J*. 1998;SPE31074:34–41.
4. Bauer A, Walle LE, Stenebråten J, Papamichos E. Impact of acidizing-induced wormholes in chalk on rock strength. In: *ARMA 13-534, Proc. 47th US Rock Mechanics/Geomechanics Symposium*. San Francisco, CA; 2013.
5. Walle LE, Papamichos E. Acidizing of hollow cylinder chalk specimens and its impact on rock strength and wormhole network structure. In: *ARMA 15-566, Proc. 49th US Rock Mechanics/Geomechanics Symposium*. San Francisco, USA; 2015.

6. Hinch EJ, Bhatt BS. Stability of an acid front moving through porous rock. *J Fluid Mech*. 1990;212:279–288.
7. Szymczak P, Ladd AJC. Instabilities in the dissolution of a porous matrix. *Geophys Res Lett*. 2011;38. L074073.
8. Zhao C, Hobbs BE, Ord A. Theoretical analyses of acidization dissolution front instability in fluid-saturated rocks. *Int J Numer Anal Methods Geomech*. 2013;37:2084–2105.
9. Liu X, Ormond A, Bartko K, Li Y, Ortoleva P. A geochemical reaction-transport simulator for matrix acidizing analysis and design. *J Pet Sci Eng*. 1997;17:181–196.
10. Valia N, Balakotaiah V. Effect of medium heterogeneities in reactive dissolution of carbonates. *Chem Eng Sci*. 2009;64:376–390.
11. Panga MKR, Ziauddin M, Balakotaiah V. Two-scale continuum model for simulation of wormholes in carbonate acidization. *AIChe J*. 2005;51:3231–3248.
12. De Oliveira TJL, De Melo AR, Oliveira JAA Jr . Numerical simulation of acidizing in carbonate reservoir. In: *CFD OIL2012, Proc. 5th Latin America CFD Workshop applied to the Oil and Gas Industry*. Rio de Janeiro, Brazil; 2012.
13. Furui K, Burton RC, Burkhead DW, Abdelmalek NA, Hill AD, Zhu D, Nozaki M. A comprehensive model of high-rate matrix-acid stimulation for long horizontal wells in carbonate reservoirs: Part I – Scaling up core-level acid wormholing to field treatments. 2012, SPE 134265.
14. Ortoleva P, Chadam J, Merino E, Sen A. Geochemical self-organization II: The reactive-infiltration instability. *Am J Sci*. 1987;287:1008–1040.
15. Chadam J, Hoff D, Merino E, Ortoleva P, Sen A. Reactive infiltration instabilities. *IMA J Appl Math*. 1986;36:207–221.
16. Ortoleva P, Merino E, Moore C, Chadam J. Geochemical self-organization I: Reaction-transport feedbacks and modeling approach. *Am J Sci*. 1987;287:979–1007.
17. Stefan J. Ueber einige Probleme der Theorie der Wärmeleitung. *Sitz ber Wien Akad Math Nat Abt*. 1889;98:473–484.
18. Ladd AJC, Szymczak P. Use and misuse of large-density asymptotics in the reaction-infiltration instability. *Water Resour Res*. 2017;53:2419–2430.
19. Ladd AJC, Szymczak P. Comment on Validity of using large-density asymptotics for studying reaction-infiltration instability in fluid-saturated rocks. *J Hydrol*. 2018;564:414–415.
20. Ciantia M, Hueckel T. Weathering of submerged stressed calcarenites: chemo-mechanical coupling mechanisms. *Géotechnique*. 2013;63:768–785. http://dx.doi.org/10.1680/geot.sip13.p.024.
21. Wangen M. Stability of reaction-fronts in porous media. *Appl Math Model*. 2013;37:4860–4873.
22. Cherniha R, Kovalenko S. Lie symmetries and reductions of multi-dimensional boundary value problems of the Stefan type. *J Phys A*. 2011;44:485202–485227.
23. Lin CC, Segel LA. *Mathematics Applied to Deterministic Problems in the Natural Sciences*. Society of Industrial and Applied Mathematics: Philadelphia; 1988.
24. Wollkind DJ, Segel LA. A nonlinear stability analysis of the freezing of a dilute binary alloy. *Phil Trans R Soc A*. 1970;268:351–380.
25. Izgec O, Zhu D, Hill AD. Numerical and experimental investigation of acid wormholing during acidization of vuggy carbonate rocks. *J Pet Sci Eng*. 2010;74:51–66.
26. Shore AF. Apparatus for measuring the hardness of materials. US patent 1770045, issued 1930-07-08.
27. Bear J. *Dynamics of Fluids in Porous Media*. Dover; 1972.
28. Schulze-Makuch D. Longitudinal dispersivity data and implications for scaling behavior. *Groundwater*. 2005;43:443–456.
29. Mathias SA. *Modelling Flow and Transport in the Chalk Unsaturated Zone* (Ph.D. thesis), University of London; 2005.